Mon. Not. R. Astron. Soc. **000**, 1–?? (2015) Printed 15 June 2016 (MN LATEX style file v2.2)

# Reorienting MHD Colliding Flows: A Shock Physics Mechanism for Generating Filaments that are Normal to Magnetic Fields

Erica Fogerty[1⋆], Adam Frank[1], Jonathan Carroll-Nellenback[1], Fabian Heitsch[2], Andy Pon[3]

[1] *206 Bausch & Lomb Hall, Department of Physics & Astronomy, University of Rochester, Rochester, New York, 14627, USA*
[2] *3255 Phillips Hall, Department of Physics & Astronomy, University of North Carolina, Chapel Hill, North Carolina, 27599, USA*
[3] *Department of Physics & Astronomy, University of Western Ontario, London, Ontario, N6A 3K7, Canada*

15 June 2016

**ABSTRACT**

We present numerical simulations of reorienting oblique shocks that form in the collision layer between magnetized colliding flows. The effect of reorientation is the alignment of post-shock filaments to be normal to the background magnetic field. We find that reorientation occurs primarily due to pressure gradients between the collision region and the surrounding environment. Our results bear striking resemblance to recent polarimetry observations of the integral filament of Taurus and filaments in Orion. Given the ubiquity of colliding flows in the interstellar medium, the process of shock reorientation provides a physical explanation for the generation of filaments that are perpendicular to magnetic fields. We find that the degree of reorientation between any two magnetized colliding flows can be formulated in terms of three upstream parameters, namely, the ratio of thermal to magnetic pressure, mach, and orientation angle.

**Key words:** *magnetohydrodynamics*(MHD) – ISM: kinematics and dynamics – ISM: structure – ISM: clouds – stars: formation

## 1 INTRODUCTION

Colliding gas flows and filaments are two structures that are commonly found in star forming regions. Converging flows have been detected surrounding molecular gas in Taurus (Ballesteros-Paredes, Hartmann & Vázquez-Semadeni 1999), the Sh 156 and NGC 7538 molecular clouds (Brunt 2003), and star forming filaments in Serpens South*. On the largest scales, they can arise from supernovae, energetic winds surrounding young stars and clusters, and the motion of galactic spiral arms through the intragalactic medium. Observational evidence supports that they even arise from cloud-cloud collisions (Looney et al. 2006; Nakamura et al. 2012). On smaller scales, converging flows can take the form of accretion flows. Similarly, filaments are ubiquitous in star forming regions. Many have been found to contain young protostellar cores*, and thus, they are considered some of the earliest structures of star formation.

How molecular clouds and their rich filamentary substructure form remains an open question in the field of star formation. One model that can easily (and self-consistently) generate filamentary molecular clouds is the colliding flows model. In this model, molecular clouds form via a variety of instabilities that occur in the post-shock region between converging flows (e.g. nonlinear thin shell, thermal, Kelvin-Helmholz and Rayleigh-Taylor instabilites, cf. Heitsch et al. (2005)). The structures that form via colliding flows tend to resemble physically-realized molecular clouds, both in terms of their morphology *and* their dynamics (Audit & Hennebelle 2005; Heitsch et al. 2006; Vázquez-Semadeni et al. 2006; Heitsch et al. 2007, 2008; Hennebelle et al. 2008; Banerjee et al. 2009; Heitsch, Stone & Hartmann 2009; Vázquez-Semadeni et al. 2011; Chen & Ostriker 2014; Körtgen & Banerjee 2015).

Recent velocity and magnetic field measurements of filaments indicate that they might be tied to colliding flows motions. Velocity measurements show that external gas motions are largely perpendicular to (and converge on) filaments*. A number of polarimetry and zeeman splitting measurements of the magnetic field indicate that the field also

⋆ E-mail:erica@pas.rochester.edu

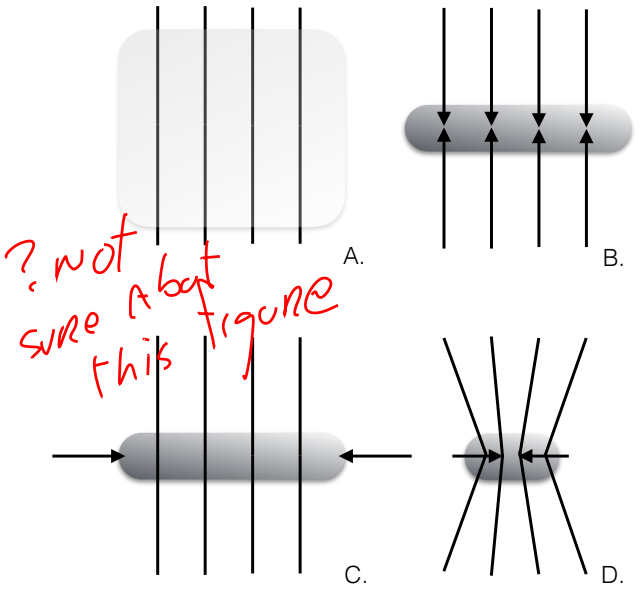


**Figure 1.** Schematic of magneto-gravitational collapse of early prestellar filaments and cores. Collapse begins with a Jeans unstable mass that is magnetically subcritical (A). Collapse proceeds along the field lines (B) until the central mass (i.e. filament, or sheet, depending on geometry) becomes magnetically supercritical. At this point, collapse can proceed along the filament, and thus, across magnetic field lines (C). This produces distortions in the magnetic field (D).

lies perpendicular to filaments*. Interestingly, fluid motions seem to change direction *inside* of filaments, so that the gas flows *along* filaments, internally*. Given that the uncertainty of polarimetry measurements increases with density, the field might actually change direction to become parallel inside of filaments as well. Indeed, if the internal field *did not* become more or less parallel to the filament, external field lines would be bent away from normal due to drag between internal fluid motions and the field (c.f. panel D., Fig. 1).

The gas motions and accompanying magnetic field geometry associated with filaments have primarily been explained through magneto-gravitational instability*. In this conceptualization, an overdense region (i.e. a core or filament within a molecular cloud) first becomes Jeans unstable (panel A., Fig. 1). Collapse is triggered and proceeds *along* magnetic field lines, as the gas is not yet magnetically supercritical (panel B., Fig. 1). Once enough mass accumulates for the central region to become magnetically supercritical, gas can begin to fall in perpendicular to the field as well. For magnetically supercritical filaments, this means collapse would then proceed *along* the filament (panel C., Fig. 1; Pon, Johnstone & Heitsch (2011); Pon et al. (2012); Toalá, Vázquez-Semadeni & Gómez (2012)). At this point, the field would become distorted as it was dragged down into the collapsing gas (panel D., Fig. 1). That the magnetic field has been shown to increase with density in collapsed gas (i.e. $B \propto n,\ n > 1000\ cm^{-3}$*; Troland & Heiles (1986); Crutcher (1999); Crutcher et al. (2010); Tritsis et al. (2015)) has commonly been cited as evidence for this scenario*.

An alternative explanation that does not require beginning with a Jeans unstable mass is a magnetized colliding flows model. Here, gas is envisioned as flowing along magnetic field lines (i.e. the path of least resistance). Overdensities form where flows collide, and these pockets of high density gas go on to become molecular clouds, or cores and filaments, depending on the flow scale. In the most general case, where the flows meet at a non-normal incidence, it has recently been found that the central shock layer readjusts so that it becomes normal to the field (and oncoming flows). This effect, which has been reported by Körtgen & Banerjee (2015) and Fogerty et al. (2016), is ~~too~~ consistent with filament gas motions and field morphology (i.e. perpendicular external and parallel internal motions, and perpendicular external field lines). Moreover, field lines that are distorted due to passage through the shocks (cf. Chen & Ostriker (2014)) exhibit a power law relationship with density consistent with the observations described above (Heitsch et al. 2007; Hennebelle et al. 2008; Banerjee et al. 2009). Thus, instead of being driven by magneto-gravitational instability, the generation of filaments perpendicular to magnetic fields (as well as the appropriate internal and external filament gas motions) can be explained by a MHD shock process - namely, the reorientation of magnetized colliding flows. This process is the topic of the present paper.

We present six models of magnetized colliding flows that exhibit varying degrees of reorientation. The effect of this reorientation is to align post-shock filaments[1] to be normal to the upstream magnetic field. In addition, we show that oblique magnetized colliding flows easily generate structures that resemble the integral filament of Orion (Bally et al. 1987; Johnstone & Bally 1999). To describe the behavior we see in our simulations, we formulate a predictive model for reorientation based on three upstream fluid variables: $\beta$ (where $\beta = P_{therm}/P_{mag}$), mach ($M$), and orientation angle of the collision interface ($\theta$).

Our paper is organized as follows. We begin with a description of our methods and numerical model (Section 2). We then discuss 1D shock solutions relevant to our work (Section 3) and our key results (Section 4). We finish with our conclusions and discussion (Section 9).

## 2 METHODS AND NUMERICAL MODELS

We ran a set of ten colliding flows simulations using AstroBEAR[2] (Cunningham et al. 2009; Carroll-Nellenback et al. 2013). AstroBEAR is a massively parallelized, adaptive mesh refinement code designed for astrophysical contexts. The numerical code solves the conservative equations of hydrodynamics and magnetohydrodynamics, and includes a wide-range of multiphysics solvers. A sampling of these solvers include self gravity, sink particles, various heating and cooling processes, magnetic resistivity, and radiative transfer. The AstroBEAR code is well tested (see, for example, Poludnenko, Frank & Blackman (2002); Cunning-

[1] In 2D, the result is actually the generation of perpendicular *sheets*. Only in 3D could true filaments form. The basic MHD shock physics described here in 2D, however, can be extrapolated to 3D. Fogerty et al. (2016), fully 3D simulations, also exhibited reorientation.

[2] https://astrobear.pas.rochester.edu

ham et al. (2009); Kaminski et al. (2014)), and is actively developed, tested, and documented by the University of Rochester's computational astrophysics group.

The present suite of simulations consisted of two sets of runs. The first was a pair of 1D shock models that investigated the wave solutions across hydrodynamic (hydro) and magnetohydrodynamic (MHD) oblique shocks, using the Exact Riemann solver and HLLD solver, respectively. The second was a parameter study of 2D magnetized colliding flows. Similar to Fogerty et al. (2016) and Haig et al. (2012), the colliding flows met at an oblique interface. The mach ($M$), $\beta$, and angle of the interface ($\theta$) was varied between the runs. The complete suite of simulations is given in Table 1.

Self-gravity was not included in the present suite of simulations. Consequently, the simulations neglect gravitational condensation along filaments. The runs therefore track the formation and early evolution of filaments, while illustrating the basic mechanism of reorientation. As we discuss in Section 9, the addition of gravity would only strengthen reorientation by adding to the effects of cooling, which was included in all of the 2D runs. The cooling prescription followed a modified II cooling curve (Inoue & Inutsuka 2008) that allowed the gas to cool to $T = 10\ K$ (Ryan & Heitsch in prep). Note, the 1D shock models did not include cooling, but instead used an adiabatic equation of state with $\gamma = 5/3$.

Each of the runs were initialized at a uniform number density of $n = 1\ cm^{-3}$ and temperature of $T = 4931\ K$. At these densities and temperatures, the gas was initially in thermal equilibrium (for those runs that included cooling). The speeds of the flows varied between $v = 11 - 73\ km\ s^{-1}$. Equivalently, the mach of the flows ranged between $M = 1.5 - 10$. These parameters were chosen to match ideal ISM conditions (as discussed in Fogerty et al. (2016)). In the 2D runs, the flows were embedded in a stationary ambient medium of the same number density and temperature. The 2D runs also included a uniform magnetic field that was parallel to the flows. The field varied in strength between $B = 1.6 - 16\ \mu G$, which is equivalent to $\beta_{plasma} = 10 - .1$. While current measurements place the global mean field of the ISM between $1 - 10\ \mu G$ (Beck 2001; Heiles & Troland 2005), we increased the field strength in some of the runs to test the effects of a stronger magnetic field on reorientation.

In 2D, the size of the domain was chosen to fully encompass fluid motions and magnetic field lines, and thus differed between the runs (cf. Table 1). However, the effective resolution was held constant at a finest cell size of $\triangle x_{min} = .15625\ pc$. Boundary conditions were set to inflow where the flows were injected, and extrapolating everywhere else. The radius of the flows was $r = 10\ pc$. In 1D, the domain was effectively infinite, with periodic boundary conditions in $y$ and inflow boundary conditions in $x$. The domain of the 1D runs had a physical length of 1 $pc$ on a side and a minimum cell size of $\triangle x_{min} = .0039\ pc$.

## 3 1D SHOCK SOLUTIONS

Before we analyze the simulations of reorienting MHD shocks, it is instructive to review the 1-dimensional wave solutions across hydrodynamic and magnetohydrodynamic oblique shocks. We begin with hydrodynamic oblique shocks.

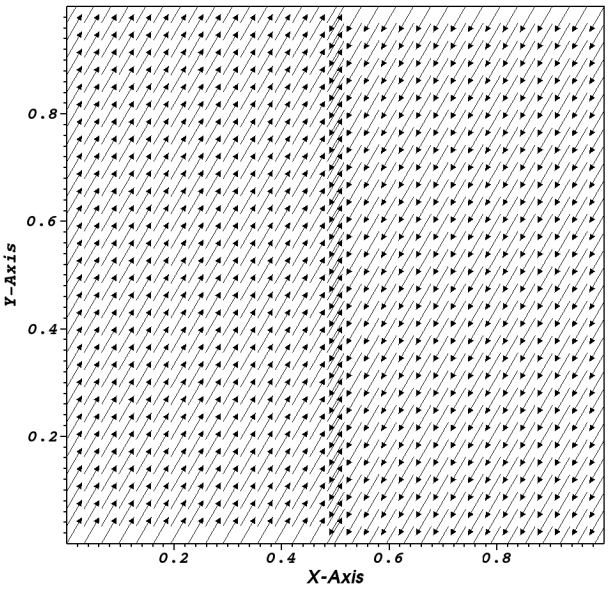


**Figure 2.** Initial condition of the 1D Riemann Problem. Incoming velocity vectors make an oblique angle with the interface (i.e. non-normal incidence). This setup is analogous to the $\theta = 30°$ finite cases discussed in Section 4, as can be seen by tilting the image by 30°. Density/pressure is constant across the interface, and when included, magnetic field lines run parallel to velocity.

### 3.1 Hydrodynamic Oblique Shocks

The 1D hydro Riemann problem relevant to the present paper consists of a constant density and pressure fluid that is separated by a discontinuous jump in velocity. In particular, the velocity field converges on the central Riemann interface at an oblique incidence (Fig. 2). Note, the angle of incidence for both the 1D hydro and MHD runs (discussed below) was chosen to be $\theta = 30°$, to match the finite $\theta = 30°$ runs of Section 4. That is, a 30° rotation puts these runs in the same frame of reference as the 2D cases presented below. This is illustrated by the top panel of Figure 3, which has been tilted by 30° for the reader's convenience.

As can be seen in Figure 3, this Riemann problem generates two oblique shocks that are separated by a contact discontinuity. In addition to the characteristic density increase across each shock front, the top panel of Figure 3 shows that the velocity vectors bend *away* from the shock normal across each shock. This occurs because only the *perpendicular* components of upstream velocity vectors ($vx$, presently) change across shocks. This leads to $vx \rightarrow 0$ in the downstream gas. Note, if $vx \neq 0$ in the post-shock gas, additional waves would be generated behind the shocks, which would violate the three-wave solution family of hydrodynamic Riemann problems. Thus, post-shock gas flows *exactly* parallel to each shock front. In other words, *oblique shocks generate shear*.

Lineouts of the various fluid variables across the wave modes are given in the bottom panel of Figure 3. First, this plot shows minor post-shock compression, consistent with the weak upstream mach of $M = 1.5$. Second, we see that the perpendicular component of velocity ($vx$) goes to zero across the shock, while the parallel component ($vy$) is unchanged. As already discussed, this leads to the generation

**Table 1.** Suite of simulations.

| Dimension | Hydro/MHD | $\beta$ | $M$ | $\theta$ (°) | Domain Length (pc) | Resolution | AMR levels |
|---|---|---|---|---|---|---|---|
| 1 | Hydro* | ... | 1.5 | 30 | 1 | $256^2$ | 0 |
| 1 | MHD* | 1 | 1.5 | 30 | 1 | $256^2$ | 0 |
| 2 | MHD | .1 | 1.5 | 30 | 160 | $256^2$ | 2 |
| 2 | MHD | 1 | 1.5 | 30 | 160 | $256^2$ | 2 |
| 2 | MHD | 10 | 1.5 | 30 | 160 | $256^2$ | 2 |
| 2 | MHD | .1 | 1.5 | 60 | 160 | $256^2$ | 2 |
| 2 | MHD | 1 | 1.5 | 60 | 320 | $512^2$ | 2 |
| 2 | MHD | 10 | 1.5 | 60 | 320 | $512^2$ | 2 |
| 2 | MHD | 1 | 10 | 30 | 320 | $512^2$ | 2 |
| 2 | MHD | 1 | 10 | 60 | 320 | $512^2$ | 2 |

*Did not include cooling

of shear, as oppositely directed $vy$ components are contiguous across the contact discontinuity. Lastly, we see that the post-shock compression is associated with a rather large increase in post-shock thermal pressure. This is due to the stiff equation of state ($P = \rho^{\gamma}$), plus the absence of cooling **EF**.

### 3.2 Magnetohydrodynamic Oblique Shocks

We now turn to magnetohydrodynamic oblique shocks, with the addition of a uniform magnetic field parallel to the flows. As stated previously, the setup was designed to match the 2D cases of Section 4. Rotating the 1D, MHD setup by 30° shows that it is the 1-dimensional analogue of the 2D, 30° runs (with the exception of cooling, which was not present in the 1D case). For the reader's convenience, this was done for the pseudocolor plot in Figure 4.

The addition of a uniform magnetic field that is parallel to the flows modifies the shock structure described in Section 3.1. A pseudocolor plot of density (Fig. 4, top panel) shows that for this case *two* oblique shocks are generated on either side of the contact discontinuity. Given Alfvén modes cannot be generated in 1D (no z-component of the magnetic field), the forward-most shock can be identified with the fast MHD shock, which is trailed by the slow MHD shock. As in the hydrodynamic model discussed above, Figure 4 shows that incoming velocity vectors are deflected *away* from the shock normal across the outer, fast shock. These redirected velocity vectors collide with the magnetic field, causing magnetic field lines to also bend away from the shock normal, given the field and fluid are perfectly coupled in ideal MHD. The inner shock is generated because the field must eventually turn back *toward* the shock normal, as it is tied to field lines across the contact discontinuity.

In addition to the bending of the field, we also see a stagnation of the velocity across the slow shock. That is, the region between the slow shocks (red region in Fig. 4, top panel) is filled with a uniform field that is kinked at its edges and has zero velocity gas motions. Note that kinking of the field increases the tension in the field at those footpoints where the field changes direction (see Fig. 4, where streamlines increase in strength from white to red), and that this kinking would be enhanced if the shocks were cooling. This is because the shocks would be thinner, and thus the angles at the footpoints would be smaller. We will explore this effect and its contribution to reorientation in Section 4. Additionally, the MHD Riemann problem must tend to the hydro solution in the limit $\beta \rightarrow \infty$. In that limit, the slow mode must collapse onto the contact discontinuity. The width of the region between the contact and the slow shock is thus a function of $\beta$. It follows that the degree of distortion (or, 'kinking') of the field is also a function of $\beta$. In Section 4, we present a model which predicts the level of reorientation based on $\beta$, as well as the shock obliquity and upstream mach.

Lineouts of the fluid variables are given in the bottom panel of Figure 4. As in Figure 3, post-shock compression across the shocks leads to strong increases in thermal pressure, due to the absence of cooling. Note that the final density and pressure over both of the shocks in the MHD case agrees with the single jump of the hydro case. This is expected, given the two solutions must converge in the limit of $\beta \rightarrow \infty$. The velocity profiles show that over the fast-shock, $vy$ increases in magnitude, while $vx$ decreases (but does not $\rightarrow 0$). Thus, over the fast shock, the flow does not become exactly parallel to the shock front, as it did in the hydro case. Instead, the flow is slightly angled toward the inner, slow-shock. This is because the gas cannot move across field lines, but rather is redirected to move along them as the shocks propagate outward. The passage of the gas through the inner, slow-shock results in the complete stagnation of the velocity. This is illustrated by both velocity components going to zero across the slow-mode. Note also the behavior of the field. The $y$-component of the field increases over the fast-shocks (becoming more parallel to the shock front), but decreases across the slow-shock (becoming more normal). This behavior is consistent with MHD fast and slow-mode shocks, in that the tangential component of the field is always amplified across fast-shocks, but decreased across slow-shocks. The $x$-component, in contrast, remains constant across the entire wave structure (again, only the tangential components of the field can change across MHD shocks).

## 4 FINITE MAGNETIZED COLLIDING FLOWS

We now turn to finite, magnetized colliding flows to address the issue of reorientation. We begin by discussing the effects of varying $\beta$ and $\theta$ on reorientation. Our analysis will then focus on the two runs that exhibited the strongest reorientation. The section is concluded with an analytical description of reorientation, as well as a comparison of our results to the

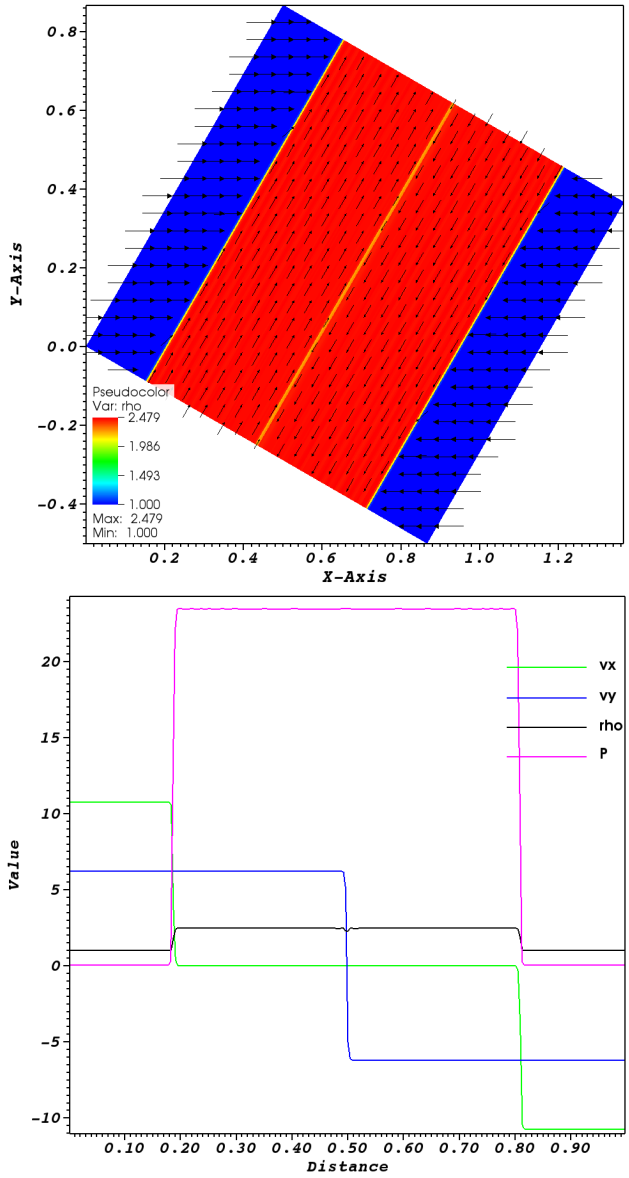


**Figure 3.** Numerical solution of the 1D hydrodynamic Riemann problem. *Top panel* is a pseudocolor plot of number density with overlaid velocity vectors. Note, the plot has been tilted by 30° so that it is in the same frame of reference as the 30° finite cases of Section 4. *Bottom panel* gives lineouts of the various fluid variables across the waves. Velocities are in units of $km/s$, number density in $cm^{-3}$, and pressure in $K/cm^3$. Pressure has been scaled to fit on the $y-$axis, where $P = (P - 4931) \times 10^{-3}$.

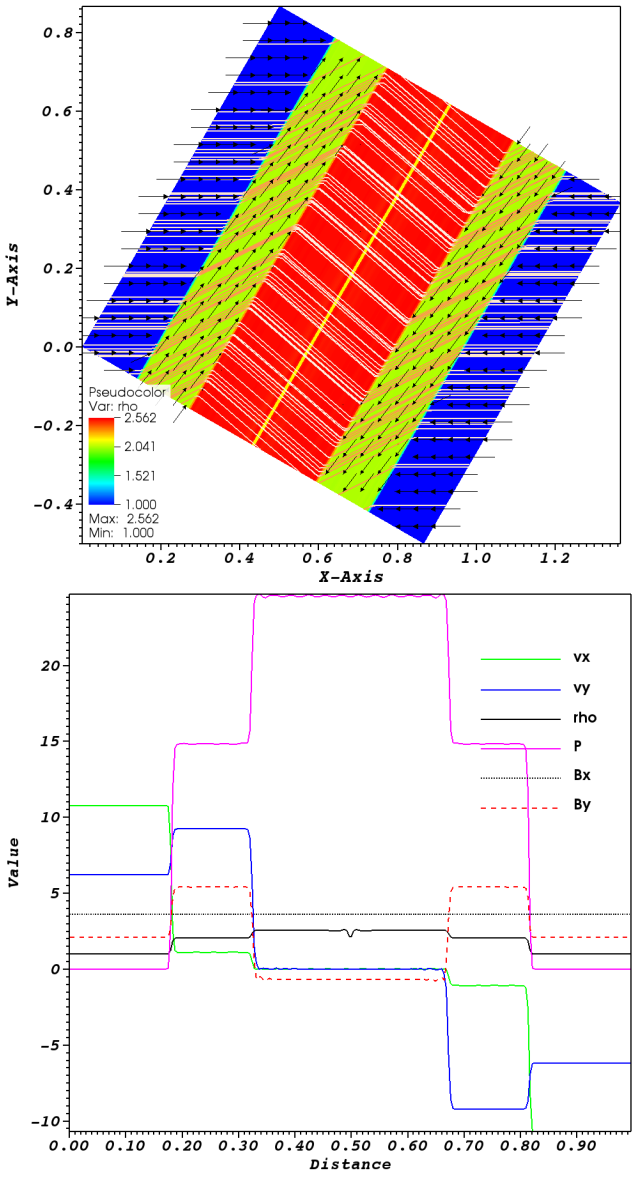


**Figure 4.** Numerical solution of the 1D magnetohydrodynamic Riemann problem. *Top panel* is a pseudocolor plot of number density with overlaid magnetic field lines and velocity vectors. Field lines increase in strength from white to red. The plot has again been tilted by 30° so that it matches the 2D 30° runs of Section 4. *Bottom panel* gives lineouts of the fluid variables across the waves. Units are the same as in Figure 3, with the addition of magnetic field components ($Bx$ & $By$), given in $\mu G$.

Orion Integral Nebula (Bally et al. 1987; Johnstone & Bally 1999).

Recall, in 1D, oblique shocks result in post-shock shear flows, with flows tracing the collision interface (Section 3). In 2D, the flows are no longer restricted to this motion. Pressure gradients that now exist between post-shock gas and the external ambient medium force material laterally outwards from the collision region. This motion straightens out the initially inclined collision region, and thus is one of the drivers of reorientation. This process is confirmed when material is *prevented* from leaving the collision region. Under such conditions, reorientation *does not* occur. Such is the case of our low $\beta$ run ($\beta = .1$), in which post-shock gas is confined to the collision region by a strong external magnetic field that runs parallel to the colliding flows. The top row of Figure 5 shows that under these conditions, material is prevented from leaving the collision region, irrespective of initial $\theta$. For these strong field cases, post-shock material continues to collect, cool, and compress over the course of the simulation ($t = 12\ Myr$), but the collision region does not change its orientation (illustrated by the black line that traces the initial collision interface in these plots). Indeed, the field is so strong in these cases that post-shock turbulence (induced from the thermal instability, e.g.) is suppressed, resulting in

the formation of a smooth and flat central filament. Magnetic field lines (overlaid in Fig. 5, top panel) are indeed resisting deformation, which would occur in the presence of a lateral flow. That is, the field lines are stiff enough to remain virtually unchanged over the course of the simulation. Moreover, the velocity vectors of the $\beta = .1$ case are aligned everywhere with the magnetic field lines. This results in *zero* post-shock shear motions, which in turn delivers material directly onto the post-shock filament that is forming. Indeed, any material that does manage to escape the collision region, travels parallel to the colliding flows, along the field lines. We call this material the 'trailing arms' of the central forming filament, and is a prominent feature of these types of flows.

The behavior begins to change as the magnetic field is weakened. When $\beta$ is increased to 1, the $\theta = 30^\circ$ case exhibits a large-scale reorientation. This is illustrated in Figure 5 (middle row, left panel), where we see a coherent, central filament has formed by $t = 6.6\ Myr$, that is more or less normal to the oncoming flows. As in the 1D version of the $\beta = 1,\ \theta = 30^\circ$ case (Section 3), an outer shock layer can be seen that diverts incoming flows either diagonally 'up' or 'down', depending on the upstream interface orientation. Across the second, inner shock layer, the flows follow the 'z-shaped' magnetic field lines, which produces a nearly parallel flow, closer-in to the filament. Note, this is in contrast to the 1D case, where internal fluid motions were absent **EF**. Near the top and bottom of the filament (i.e. near the flow-ambient boundary) and across the collision interface, the velocity vectors become aligned so that they are pointing radially outwards. That is, the flow switches from being a shear flow across the fast-shock, to being directed outwards into the ambient medium. This is again due to pressure gradients that exist between the collision region and the ambient medium in *finite* colliding flows. The ejection of material from the over-pressurized collision region into the ambient medium produces arcs in the magnetic field lines, whose tension impedes further lateral flow, and traps the ejected gas. This trapped gas travels along the magnetic field line arcs, as shown by the corresponding velocity vectors in Figure 5. Such magnetic field line arcs were discussed and described analytically in Fogerty et al. (2016). Lastly, we see the formation of a weak 'mirror image' of the trailing arms, which are forming due to the collection of ejected material into the arcs defined by the magnetic field.

A bit more discussion on the magnetic field structure of this case is in order. Looking again at the middle, left panel of Figure 5, we can at once see regions where the field is experiencing strain. This is given by the color of the field lines, which increase with field strength from white to black. From this figure, we see that the field increases in strength across shocks, as well as in the arcs above and below the ejection region. This is due to increased magnetic tension and pressure from both the post-shock flow and ejecta colliding with field lines. In a similar manner, cooling, which is driving flow onto the central forming filament, is producing amplification of the field closer-in to the filament. The overarching result of this post-shock flow pattern is to produce field lines that enter the outer shock layer (i.e. outer layers of the filament) at a nearly normal incidence, but that tend toward a parallel orientation between the fast shocks (albeit in opposite directions across the slow shocks and contact). Moreover, this 'z-shaped' magnetic field structure, characteristic of oblique magnetized colliding flows, persists even after the shocks themselves have reoriented (as can be seen in the figure). Lastly, note the central filament is forming between regions of highest magnetic support, a point we will return to in later sections. **EF**.

As the inclination angle steepens to $60^\circ$ for the $\beta = 1$ case, we see the same trends develop as the $30^\circ$ case. Namely, we see the deflection of material away from the shock normal across a fast, outer shock, an ejection of material away from the collision region, and a central "s"- shaped filament form that has undergone a similar degree of reorientation. With regards to the magnetic field geometry, we again see that the filament has formed in regions of locally suppressed magnetic field strength, in-between highly strained magnetic field lines. However, the higher obliquity shocks of this run produces overall wider shocks. This is due to weaker post-shock compression, given the lowered 'effective' mach of this run, which leads to weaker cooling, and hence greater post-shock thermal support (i.e. wider shock fronts).**EF**. Again, tracing the magnetic field lines (see Fig. 5, middle row, right panel), the flow transitions from entering the outer shock of the filament at a normal incidence, to becoming highly parallel to the filament just along its boundary (i.e. within the slow shock).

As the field is weakened more to $\beta = 10$, even less magnetic support is afforded to the post-shock region. This is evidenced by a further-reaching lateral expansion of material away from the collision region (i.e. weaker tension in the magnetic arcs), as well as the slow shocks having collapsed virtually entirely onto the central contact discontinuity (Fig. 5, bottom left and right panels). Indeed, the flow enters the fast, outer shock, is deflected away from the shock normal, and then continues along until it collides with the central growing filament. The field lines follow this behavior. They enter the fast outer shock, are bent away from the shock normal, and then sharply change direction along the contact discontinuity to connect with field lines across the shock. Similar to previous runs, both the $\theta = 30^\circ$ and $60^\circ$ cases are s-shaped (or 'integral' shaped), with trailing arms that protrude from the collision region, and both have exhibited varying degrees of reorientation. The $60^\circ$ case, having been run out to longer times, shows a more complete degree of reorientation (Fig. 5, bottom-right panel). Note the KH-like instabilities forming in the trailing arms of the $60^\circ$ run. Given the simulations are 2D, the size-scale of these instabilities may be unphysical, given the inverse cascade* of turbulence in 2D.

## 5 TEMPORAL EVOLUTION OF REORIENTING FLOWS

In this section we briefly describe the temporal evolution of reorienting colliding flows, before moving on to our central analysis of the $\beta = 1,\ \theta = 30^\circ$ and $60^\circ$ cases.

### 5.1 $\beta = 1$, $\theta = 30^\circ$

Figure 6 shows the evolution of the $\beta = 1,\ \theta = 30^\circ$ case. As in the 1D version of this run (Section 3), the field is strong enough to support both a fast shock and a well-defined slow

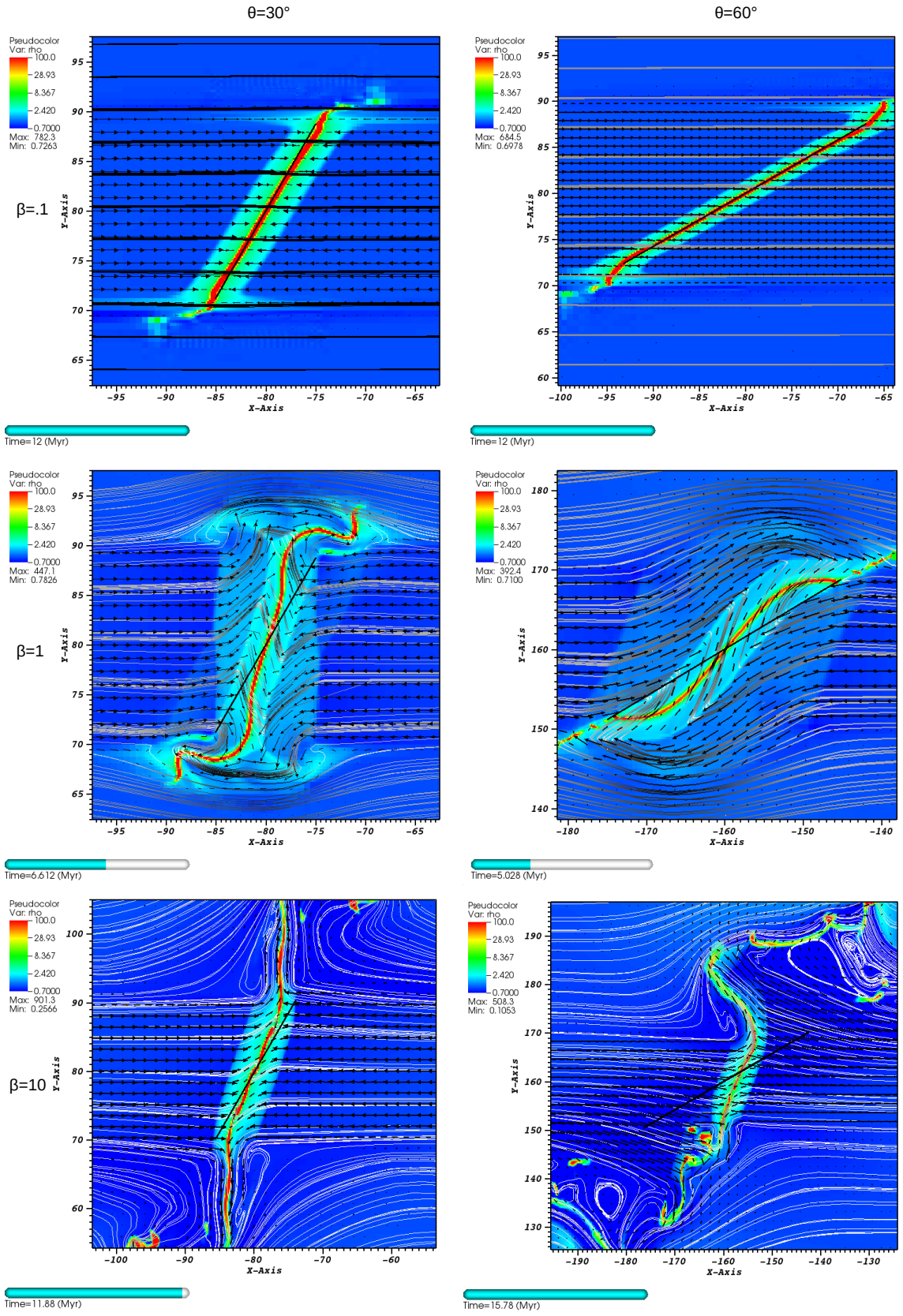


**Figure 5.** Density pseudocolor plots with overlaid velocity vectors and magnetic field lines. The legend gives number density in units of $cm^{-3}$. Velocity vectors are scaled by magnitude, and field lines increase in strength from white to black. *On left* are the 30° runs, which increase in $\beta$ from top to bottom. *On right* are the 60° runs, which also increase in $\beta$ from top to bottom. The black reference line traces the initial collision interface of the given run.

shock (compared to the weaker field cases, where the slow shock is virtually absent, see below). The presence of the slow shocks in this case provides a larger distance over which magnetic field lines can change direction. As can be seen in the $t = .49\ Myr$ panel, the bulk properties of the flow are similar to the 1D case, at early times. That is, a shear flow is established across the outer, fast shock, and negligible fluid motions occur inside of the slow shocks. Over time, post-shock cooling triggers inflow along the field lines onto a centrally forming filament ($t = 2.1\ Myr$). Additionally, this time panel shows that the fast shock has stalled near the flow-ambient boundary, on the side of the interface closest to the forming filament. This is due to a decrease in thermal pressure support as material is ejected away from the collision region, resulting in the outer shock layer becoming normal to the oncoming flow.

As can be seen in the figure (and even better in the animations online[3]), reorientation begins with the lateral ejection of material from the collision region ($t = .49\ Myr$ panel). This produces sections of the filament that are normal to the oncoming flows, nearest the flow-ambient boundary ($t = 2.1\ Myr$). Over time, this reorientation moves downward, toward the center of the filament ($t = 12\ Myr$). This is due to the combined effect of the stalled outer shock front, as well as internal magnetic tension. Lastly, note that both the inner and outer shocks persist over the entire course of the simulation, but that additional weak shocks form at the outer boundary of the filament, as internal shock layers and field lines adjust to reorientation.

### 5.2 $\beta = 10$, $\theta = 30^\circ$

The $\beta = 10,\ \theta = 30^\circ$ case starts out similar to the $\beta = 1$ case, in that a strong outflow is set up early on from the collision region into the ambient gas (see the $t = .53\ Myr$ panel of Fig. 7). However, there are a couple of notable differences. First, the post-shock region is bounded by only two shocks (as opposed to four). Second, this causes a greater distortion of the field lines, as the single shocks result in a stronger shear flow. This can be seen by the sharper turns of the post-shock field lines at this point in the simulation (i.e. the formation of the characteristic 'z-shape' field structure). By $t = 3.1\ Myr$, internal field lines are being heavily strained, as they are stretched into a near vertical orientation. These field lines are shaded black in the figure, which indicates they are undergoing the greatest amplification in the flow. The enhanced field strength in this region resists accumulation of gas onto the central filament axis. Instead, material begins to collect around the top and bottom of the filament, as well as the outside, in a 'rubber-band'-like shape. Ejecta continues to push out into the ambient environment, dragging field lines along with it.

By $t = 6\ Myr$, gas has successfully collapsed onto the central axis, and the filament is growing in density, albeit with a strong central, parallel magnetic field component. The flow is again parallel to the central axis within the shock-bounded filament, and the entire structure (filament + trailing arms) has assumed an integral, or s-shaped, geometry. By the last frame ($t = 12\ Myr$), peak densities have continued to rise, and we see the onset of fluid instabilities (i.e. KH and cooling), along the central ridge of the filament.

### 5.3 $\beta = 1$, $\theta = 60^\circ$

As in the $\beta = 1,\ \theta = 30^\circ$ case, the strong field again fully supports the four-shock structure characteristic of magnetized colliding flows (Fig. 8). The steeper inclination angle of the $\theta = 60^\circ$ case, however, results in a lower effective upstream mach, and thus 'puffier' shocks. There is also less bending of magnetic field lines, given the weaker shocks. At early times ($t = 1.1\ Myr$), field lines that enter the collision zone from the left, drop down vertically to connect to field lines across the contact discontinuity. Between the slow shocks (green region), the field is fairly constant, and there is negligible fluid motions along them.

By $t = 2.3\ Myr$, gas is beginning to fall onto the central filament axis, as material is shocked and cooled. Also, internal field lines begin to show strain, marked by the transition of field lines from white to black. A closer look shows that field lines are in fact beginning to stretch past their initial vertical orientation, due to the shear flow, consistent with field amplification **EF**. Additionally, the outer shocks have already begun to stall, resulting in the reorientation of the outer shock layer. Lastly, by $t = 2.3\ Myr$, trailing arms that flank the filament have begun to develop. These are being generated by material entering the collision region from the right and left that is being quickly shunted away by the oblique shocks diagonally down and up, respectively. Given the strength of the magnetic field in this case, shunted material is unable to escape to large distances from the filament. Rather, it reaches some characteristic radius before falling back along the field lines toward the colliding flows. Fogerty et al. (2016) showed that this characteristic radius can be written as:

$$r \approx \frac{\sqrt{\beta_{ram}}R}{2}$$

where $\beta_{ram} = \rho v^2 (B^2/2)^{-1}$, and $R$ is the colliding flows radius. For our parameters here ($\beta_{ram} = 3.8$), this gives $r \approx R$, which is in good agreement with the arcs after the flow has reached a quasi-steady state (see Fig. 8, $t = 6.4\ Myr$ panel).

By $t = 4.4\ Myr$, there is a well-defined, high density filament, and the trailing arms have become more prominent. Taken together, an integral-shaped filament has formed. Within the highest density regions of the filament, field lines continue to stretch and grow in strength. By $t = 6\ Myr$, the main component of the s-shaped filament has reoriented. Animations of this run show that only the main body of the filament undergoes reorientation, as it is squeezed between stretched field lines. Note, we stop the simulation at this point as instabilities begin to develop in the outer shock layers that are unphysical in 2D, given the inverse cascade.

### 5.4 $\beta = 10$, $\theta = 60^\circ$

To conclude this section, we address how weakening the field in the $\theta = 60^\circ$ case changes the flow evolution. As we have

[3] See the online supplementary material, as well as the following youtube channel: https://www.youtube.com/channel/UCEmUg0BdCyPC3QnKdNDJq1w

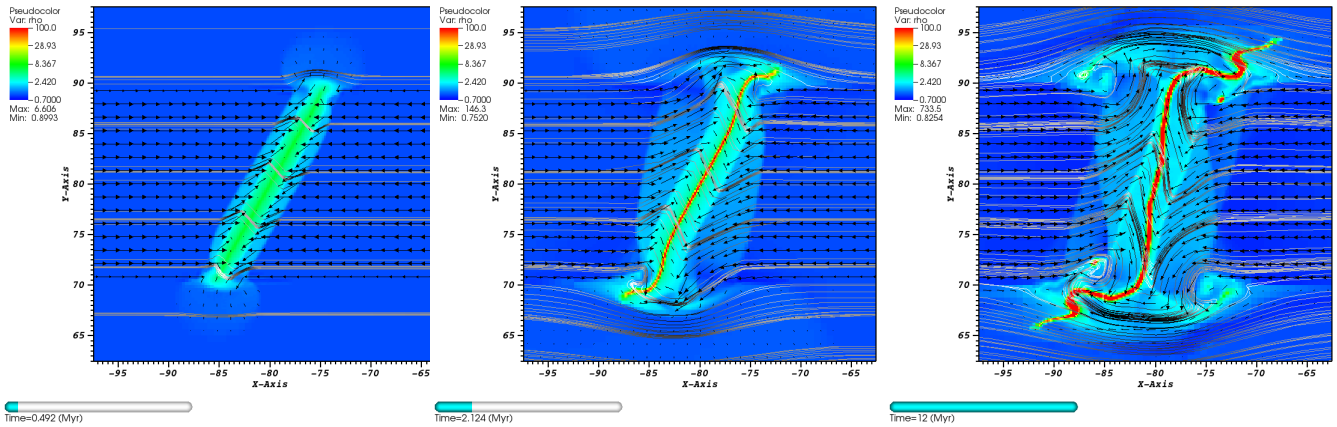


**Figure 6.** Evolution of the $\beta = 1,\ \theta = 30^\circ$ case. All units and are the same as in Figure 5.

seen in the $\beta = 10, \theta = 30^\circ$ run, decreasing the strength of the field leads to a single shock jump on either side of the contact discontinuity. Across this jump, the field lines are deformed to a greater extent, due to the weaker nature of the field and the more extreme shear flow that results from a collapsed slow shock (Fig. 9, $t = .46\ Myr$ panel). The ability of the field lines to stretch to a greater extent leads to regions of extreme tension in the field, so strong that the inner regions of the forming filament are vacated of gas ($t = 1.8\ Myr$). At this point in the evolution, trailing arms begin to form, as well as stalled shock fronts. As time goes on, thermal pressure gradients of compressed and cooling post-shock gas exceed magnetic pressure and tension forces, and the filament begins to take shape ($t = 4.3\ Myr$). Note that the filament forms from the outside-in, meaning from the ambient medium toward the center of the collision region. This coincides with those regions of the filament that also happen to be normal to the flows. By the last frame ($t = 15.8\ Myr$), there is a torque being generated on the center filament, visible by the mismatch of velocity vectors on opposite sides of the interface. We are left with a normal filament to the background flows and magnetic field, that has a parallel flow field internally. Note, this simulation was run out the longest, as reorientation proceeded slower in this case (see the online animations for more detail).

## 6 PRESSURE GRADIENTS AND MAGNETIC FORCES DRIVE REORIENTATION

As suggested in the previous section, pressure gradients and magnetic forces become dominant drivers of reorientation under different dynamical scenarios. In this section, we analyze two archetypal models, the $\theta = 30^\circ$, $\beta = 1$ and $\beta = 10$ cases, in order to further characterize these main drivers of reorientation.

## 7 ANALYTICAL DESCRIPTION OF REORIENTATION

We now turn to building a single, simple model of reorientation based on the results of the previous section. As we will show, this model can describe reorientation using three key parameters: $\beta$, $\theta$, and $M$.

## 8 CONNECTIONS TO THE INTEGRAL FILAMENT AND OTHER RECENT OBSERVATIONS

The 'integral-shaped filament', first characterized by Bally et al. (1987), is an s-shaped filament in the northern region of the Orion A molecular cloud. It is the nearest site of active star formation, at only 50 parsecs away*. A column density map of this filament is shown in Figure.

## 9 DISCUSSION

## ACKNOWLEDGMENTS

This research was supported through grant GR523126, as well as the National Science Foundation through grant GR506177, and the Space Telescope Science Institute through grant GR528562.

## REFERENCES

Audit E., Hennebelle P., 2005, A&A, 433, 1
Ballesteros-Paredes J., Hartmann L., Vázquez-Semadeni E., 1999, , 527, 285
Bally J., Langer W. D., Stark A. A., Wilson R. W., 1987, ApJl, 312, L45
Banerjee R., Vázquez-Semadeni E., Hennebelle P., Klessen R. S., 2009, MNRAS, 398, 1082
Beck R., 2001, SSRv, 99, 243
Brunt C. M., 2003, , 583, 280
Carroll-Nellenback J. J., Shroyer B., Frank A., Ding C., 2013, Journal of Computational Physics, 236, 461
Chen C.-Y., Ostriker E. C., 2014, ApJ, 785, 69
Crutcher R. M., 1999, ApJ, 520, 706
Crutcher R. M., Wandelt B., Heiles C., Falgarone E., Troland T. H., 2010, ApJ, 725, 466
Cunningham A., Frank A., Varnire, P. M. S., Jones T., 2009, ApJS, 182, 519

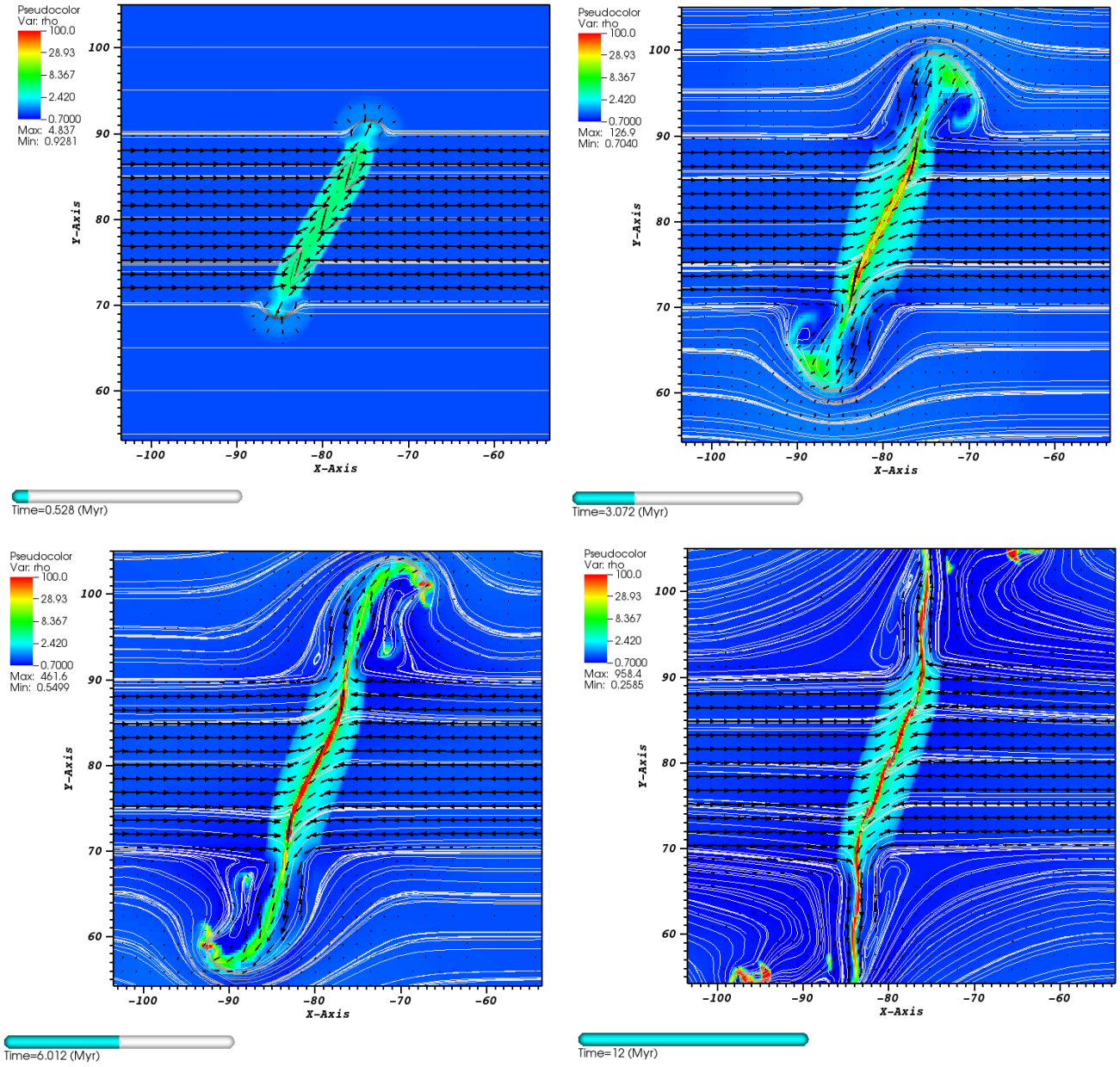


**Figure 7.** Evolution of the $\beta = 10,\ \theta = 30^{\circ}$ case. All units and are the same as in Figure 5.

Fogerty E., Frank A., Heitsch F., Carroll-Nellenback J., Haig C., Adams M., 2016, ArXiv e-prints

Haig C. M., Heitsch F., Carroll J., Frank A., 2012, in American Astronomical Society Meeting Abstracts, Vol. 219, American Astronomical Society Meeting Abstracts #219, p. 349.02

Heiles C., Troland T. H., 2005, ApJ, 624, 773

Heitsch F., Burkert A., Hartmann L., Slyz A. D., Devriendt J. G., 2005, ApJ, 633, L113

Heitsch F., Hartmann L. W., Slyz A. D., Devriendt J. E. G., Burkert A., 2008, ApJ, 674, 316

Heitsch F., Slyz A. D., Devriendt J. E. G., Hartmann L. W., Burkert A., 2006, ApJ, 648, 1052

Heitsch F., Slyz A. D., Devriendt J. E. G., Hartmann L. W., Burkert A., 2007, ApJ, 665, 445

Heitsch F., Stone J. M., Hartmann L. W., 2009, ApJ, 695, 248

Hennebelle P., Banerjee R., Vázquez-Semadeni E., Klessen R. S., Audit E., 2008, A&A, 486, L43

Inoue T., Inutsuka S.-i., 2008, ApJ, 687, 303

Johnstone D., Bally J., 1999, ApJl, 510, L49

Kaminski E., Frank A., Carroll J., Myers P., 2014, ApJ, 790, 70

Körtgen B., Banerjee R., 2015, , 451, 3340

Looney L. W., Wang S., Hamidouche M., Safier P. N., Klein R., 2006, , 642, 330

Nakamura F. et al., 2012, ApJ, 746, 25

Poludnenko A. Y., Frank A., Blackman E. G., 2002, , 576,

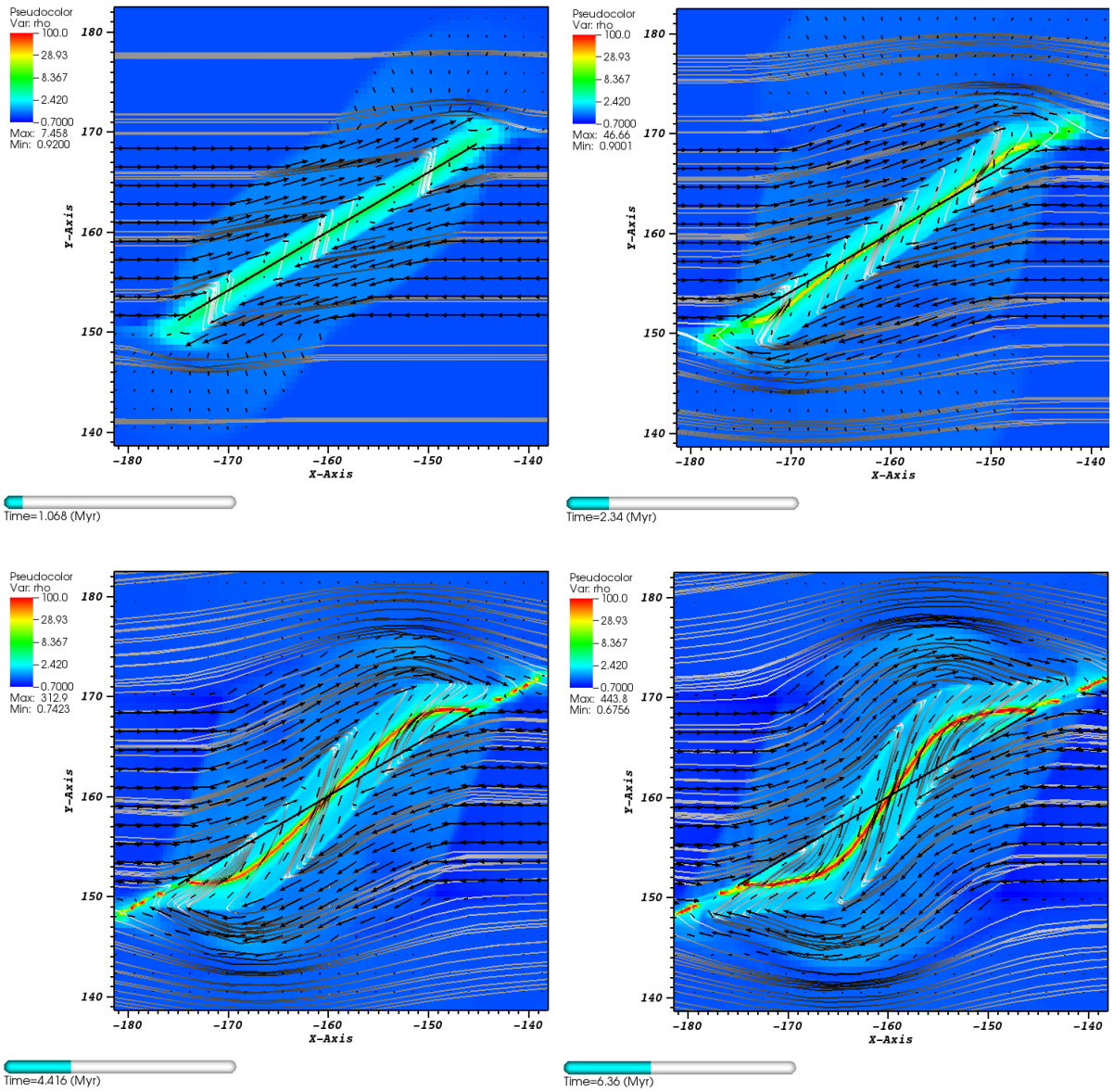


**Figure 8.** Evolution of the $\beta = 10$, $\theta = 60°$ case. All units and are the same as in Figure 5. A black reference line has been added that traces the initial collision interface.

832
Pon A., Johnstone D., Heitsch F., 2011, ApJ, 740, 88
Pon A., Toalá J. A., Johnstone D., Vázquez-Semadeni E., Heitsch F., Gómez G. C., 2012, ApJ, 756, 145
Toalá J. A., Vázquez-Semadeni E., Gómez G. C., 2012, ApJ, 744, 190
Tritsis A., Panopoulou G. V., Mouschovias T. C., Tassis K., Pavlidou V., 2015, MNRAS, 451, 4384
Troland T. H., Heiles C., 1986, ApJ, 301, 339
Vázquez-Semadeni E., Banerjee R., Gómez G. C., Hennebelle P., Duffin D., Klessen R. S., 2011, , 414, 2511
Vázquez-Semadeni E., Dongsu R., Passot T., Gonzalez R. F., Gazol A., 2006, , 643, 245

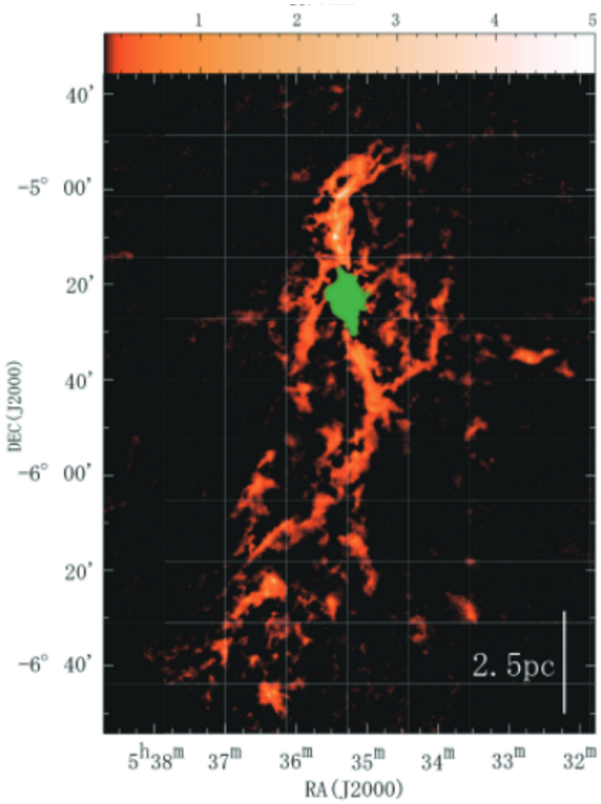


**Figure 9.** The Integral-Shaped Filament.